Progress In Electromagnetics Research C, Vol. 15, 187–199, 2010

A NOVEL SIGNAL INTEGRITY METHODOLOGY BY 3D DIRECT ANALYSIS FOR MICROWAVE TESTING PROBES

S.-M. Wu and S.-W. Guan

Department of Electrical Engineering
National University of Kaohsiung
No. 700, Kaohsiung University Rd., Nan-Tzu Dist.
Kaohsiung, Taiwan, R.O.C.

Abstract—This research uses innovative approaches for characterizing spring probes, a final-test bottleneck applied to microwave packaging. The modeling method depends on conventional microwave on-wafer measurement. This paper compares the novel microwave 3D direct calibration and measurement to observe the issues of spring probe reliability. We makes the key component of a novel approach to 3D calibration and measurement, the double-sided thru calibration element with delay time delivers from 3D EM simulation. The current study compares the modeling method and 3D direct measurement to prove the capability of the latter and presents the reliability about compressing distance of spring probes.

1. INTRODUCTION

Increasingly high-speed serial I/Os are available in mobile products operating at gigabit data rates, creating significant challenges not only for silicon providers, but also for the Automated Testing Equipment (ATE) industry. The ATE provides a methodology for transmitting signals to and from the device under test (DUT) to the tester. The critical challenge is maintaining the signal integrity between the ATE instruments and the DUT.

The spring probe type assemblies have been a standard interface in the ATE industry, consisting of an adjustable length spring applied to the spring probe that ensures a good connection. The electromagnetic

---

Received 7 June 2010, Accepted 4 August 2010, Scheduled 14 August 2010

Corresponding author: S.-M. Wu (sungmao@nuk.edu.tw).

coupling between pins creates crosstalk noise, and a repeatedly pressed spring is unstable. Previous studies have discussed the impedance and delay time of several spring probe types [1]. Novel high-speed and ultra high speed spring probe types have been developed [2–4]. Subsequently, the crosstalk noise between spring probes has become the most critical signal integrity issue for high-speed digital systems. Enlarging the pin pitch of spring probe structures reduces crosstalk noise. The current advanced systems with high-density pads do not have this capability. We seek to increase the bandwidth of the spring probe interface.

The modeling method presented in Section 2 is complex and imprecise. The characteristic performance of the spring probe requires many fixtures to achieve the open and short circuits at the terminal of spring probe that creates and de-embeds the equivalent model attaining real performance of the spring probe [5, 6]. The parasitic effect of fixtures could be larger than spring probe in most cases, and the ground loop inductance has been ignored when shorting the terminals of spring probes and results in the distortion of an equivalent model.

A novel 3D on-wafer measurement is developed in the paper that modifies conventional calibration thru element to become that novel double-side element. The advantages of this approach are that it is simple, quick and accurate without cumbersome mathematical processes. This measurement technique will be a critical solution for any vertical transmission structure and transient issues [7, 8].

2. MODELING METHOD

The RF spring probes characteristics have been realized with load boards or test fixtures from the ATE industry. The response of the whole structure is obtained by this approach. The real characteristic of spring probe section cannot be obtained, because of de-embedding of transmission lines, adaptors, and vias. The approach used creates the schematic equivalent model by curve fitting several test fixtures. A modeling method that includes complex mathematical operations and model optimization is presented. Notice that test fixtures with parasitical effects will limit the bandwidth of an equivalent model. The modeling method is presented below.

The whole structure is presented in Fig. 1 and divided into three parts. The PCB board represents the adapter between RF probes and spring probes for probing space and transmitting signals into spring probes with vias as shown in Fig. 2(a). Next, for the spring probe, the test board allows the terminals of spring probes to become an open

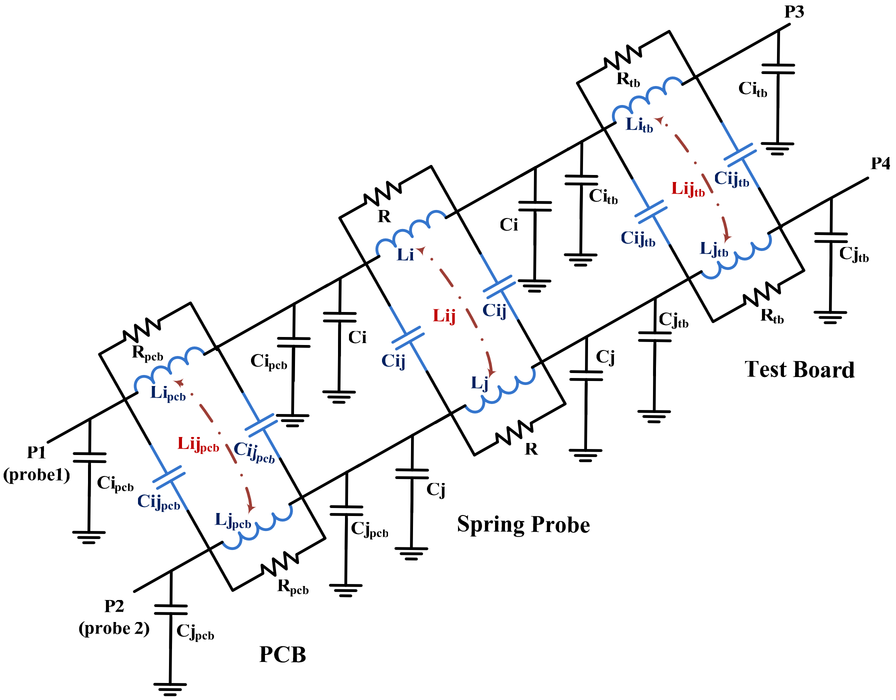

Figure 1. Basic equivalent Model of spring probes and fixtures.

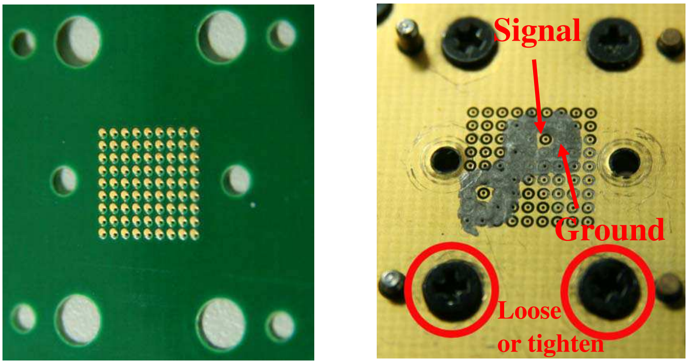

(a) (b)

Figure 2. (a) Spring probe side of text fixture. (b) Probing side of test fixture.

or short circuit. Conductive silver paste is coated on the backside as shown in Fig. 2(b). These three parts are similar and simplified into two signal paths, port 1–port 3 and port 2–port 4. Each path contains a series of main inductors (L_i, L_j) and two external inductors (L_{ipcb}, L_{jpcb}; L_{itb}, L_{jtb}). The lossy components and mutual inductances have been considered for every inductor and for the electrical coupling between the two paths. Couplings between the signal path and ground are considered parallel capacitors. This model can be applied to both differential modes and single-end transmissions. The single-end mode is considered one signal pin and one ground pin and will be grounded at port 2 and port 4.

Consideration of each cell in the model is shown in Fig. 3(a). The first opened is port 3, while port 4 delivers only one port response. This model can be simplified into two parallel capacitors at a low frequency. All lossy components will be considered at the final stage of this modeling method. The S_{11} with an open path is presented in Eq. (1). Notice that port 2 is terminated at this time.

$$S_{11}^{op}=\frac{1-j\omega Z_0(C_i+C_{ij})}{1+j\omega Z_0(C_i+C_{ij})}=\frac{1-[\omega Z_0(C_i+C_{ij})]^2}{1+[\omega Z_0(C_i+C_{ij})]^2}-j\frac{2\omega Z_0(C_i+C_{ij})}{1+[\omega Z_0(C_i+C_{ij})]^2} \tag{1}$$

For calculation, Eq. (1) is changed into following equation.

$$\tan(-\angle S_{11}^{op})=\frac{2\omega Z_0(C_i+C_{ij})}{1-[\omega Z_0(C_i+C_{ij})]^2} \tag{2}$$

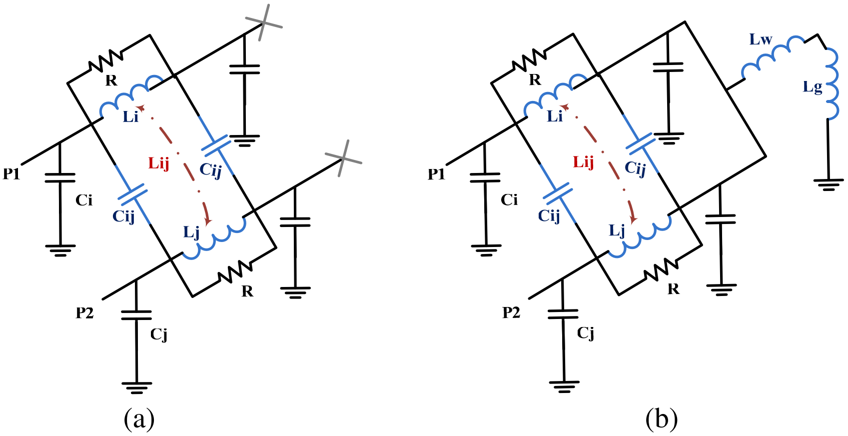

Figure 3. (a) Simplified model with open path. (b) Simplified model with short path.

The second term of denominator in Eq. (2) is less than 1, because the order of C_i and C_{ij} is -12, and ω is 9. Eq. (2) can be simplified into Eq. (3) when the second term of denominator is ignored.

$$\tan(-\angle S_{11}^{op}) = 2\omega Z_0(C_i + C_{ij}) \tag{3}$$

The expression of C_i and C_j can be found in Eqs. (4), (5).

$$C_i = \frac{\tan(-\angle S_{11}^{op})}{2\omega Z_0} - C_{ij} \tag{4}$$

$$C_j = \frac{\tan(-\angle S_{22}^{op})}{2\omega Z_0} - C_{ij} \tag{5}$$

Consider the effects between ports 1 and 2, the model at low frequency can be simplified into C_{ij} that connects the two ports. Delivering the ABCD matrix of C_{ij} and changing into a scattering matrix, the S_{12} with an open path is shown in Eq. (6).

$$S_{12}^{op} = \frac{2j\omega Z_0 C_{ij}}{1 + 2j\omega Z_0 C_{ij}} = \frac{4\omega^2 Z_0^2 C_{ij}^2}{1 + 4\omega^2 Z_0^2 C_{ij}^2} + j\frac{2\omega Z_0 C_{ij}}{1 + 4\omega^2 Z_0^2 C_{ij}^2} \tag{6}$$

The expression of C_{ij} is delivered in Eq. (7).

$$C_{ij} = \frac{1}{4\pi f Z_0}\sqrt{\frac{|S_{12}^{op}|^2}{1 - |S_{12}^{op}|^2}} \tag{7}$$

The previous model in Fig. 3(b) shows that the short path at ports 3 and 4 occur at external inductances, L_w and L_g. L_w suits to the wire bonding to ground at the package level modeling, and L_g represents ground inductance of the short path. Conventionally, L_w and L_g are ignored and assumed the sampling at low frequency. This assumption limits the model's bandwidth. The conductive silver paste has been coated on the probing side of test board to achieve a short path and combine parasitical effects of conductive pastes with ground inductance into L_g. Repeatedly terminating port 2 to show S_{11} in the simplified model at low frequency.

$$S_{11}^{sp} = \frac{Z_{in} - Z_0}{Z_{in} + Z_0} = \frac{\omega^2(L_i + L_g) - Z_0^2 + 2j\omega(L_i + L_g)Z_0}{\omega^2(L_i + L_g)^2 + Z_0^2} \tag{8}$$

Eq. (8) is changed into Eq. (9) for the calculation.

$$\tan(\angle S_{11}^{sp}) = \frac{2\omega(L_i + L_g)Z_0}{\omega^2(L_i + L_g) - Z_0^2} \tag{9}$$

Table 1. Parameters of whole model.

C_{ij}	57.456 fF	C_{ijpcb}, C_{ijtb}	5.728 fF
C_i, C_j	90 fF	C_{ipcb}, C_{jpcb}, C_{itb}, C_{jtb}	140 fF
L_{ij}	0.858 nH	L_{ijpcb}, L_{ijtb}	0.02 nH
L_i	1.8 nH	L_{ipcb}, L_{itb},	0.27 nH
L_j	1.8 nH	L_{jpcb}, L_{jtb}	0.18 nH
Mutual K	0.477	Mutual K_{pcb}, K_{tb}	0.077

L_i and L_j are found in the following:

$$L_i = \frac{Z_0}{2\pi f}\frac{1+\sec(\angle S_{11}^{sp})}{\tan(\angle S_{11}^{sp})} - L_g \tag{10}$$

$$L_j = \frac{Z_0}{2\pi f}\frac{1+\sec(\angle S_{22}^{sp})}{\tan(\angle S_{22}^{sp})} - L_g \tag{11}$$

The way to analyze the mutual inductance between L_i and L_j has been replaced by T model and simplified to the series of L_{ij} and L_g.

$$S_{21}^{sp} = \frac{2}{2+\frac{Z_0}{j\omega(L_{ij}+L_g)}} = \frac{4\omega^2(L_{ij}+L_g)^2 + 2j\omega(L_{ij}+L_g)Z_0}{Z_0^2 + 4\omega^2(L_{ij}+L_g)^2} \tag{12}$$

The mutual inductance is delivered in Eq. (13).

$$L_{ij} = \frac{Z_0}{2\omega}\left|S_{21}^{sp}\right| - L_g \tag{13}$$

Most components of the cell model in Figs. 3(a), 3(b) have been delivered by remaining lossy with capacitors obtained by optimizing the model in EDA tools that fit for the measurement data. This modeling method is based on Fig. 1, which includes the PCB, spring probe and test board. Before extract the parameters of spring probe, the parasitical effects of PCB and test board must be de-embed from Fig. 1. The characteristics of spring probes are indirectly accessed by characterizing PCB and test board by the same modeling steps mentioned above. All parameters of whole model in Fig. 1 are presented in Table 1.

3. NOVEL 3D DIRECT MEASUREMENT

3.1. Measurement Environment Introduction

Novel 3D calibration and measurement model achieves standard SOLT [9] calibration. There is a special issue with the “thru”

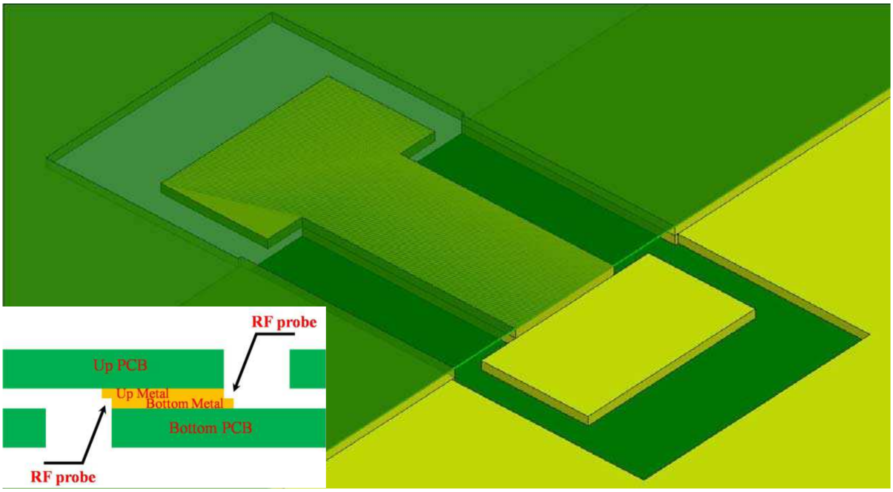

Figure 4. Cross-section diagram of novel double-side thru element.

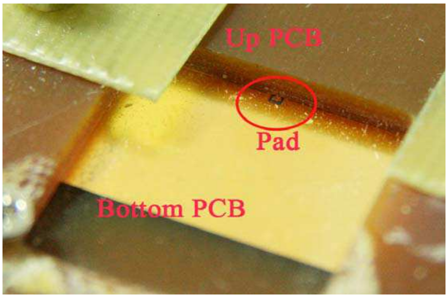

Figure 5. Two pieces of PCB combine into double-side thru element.

calibration element. The "thru" element must be re-designed in order to be the probe below and above the sides simultaneously. The basic structure of double-side thru element is presented in Fig. 4 and contains two separate PCBs stacked face-to-face with each PCB slotted to expose copper layer for the probing. There is 0.75 mm length, 250 μm width, and 155 μm spacing for the CPW transmission line on each PCB with Nelco N4000 dielectric, and the thickness of each single copper layer is 20 μm. By combining the two PCBs, they become a 0.5 mm 50 ohm CPW line embedded in dielectrics with two opposite-oriented 0.25 mm pads exposed to the air as shown in Fig. 5. There are two issues that involve impedance control and adhesion between the two PCBs that must be taken care of. The width and spacing of the exposed pad are 425 and 75 µm. The difference between the conventional and novel double-side thru element approach is that it contains two dielectric layers and embeds the CPW.

The standard definition is the core of each calibration method, and the accuracy of the calibration depends on the thru element to be redesigned and modified. The parameter that relates to the thru element is thru delay and is explicitly definite to calculate error terms and avoid over-calibration. The double-side thru element has been simulated in a 3D EM solver, and the thru delay is given by Eq. (14) [10].

$$delay = \frac{-\{\arg[S_{21}(f)] - \arg[S_{21}(0Hz)]\}}{360 * f} \tag{14}$$

The unit of $\arg(S_{21}(f))$ is degrees and considered at 1 GHz, but can be used to every frequency as the linearity of thru element is questioned. According to double-side thru element simulation results

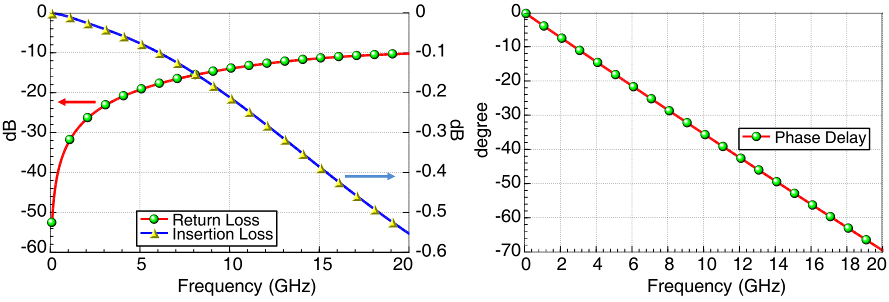

(a) (b)

Figure 6. (a) Return loss and insertion loss of simulated double-side thru element. (b) Phase delay of simulated double-side thru element.

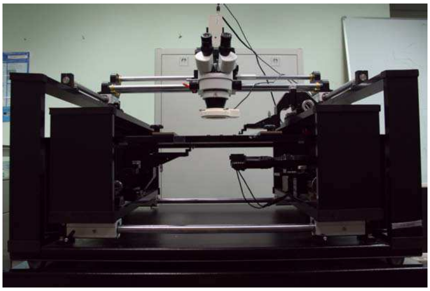

Figure 7. Customized double-side probe station.

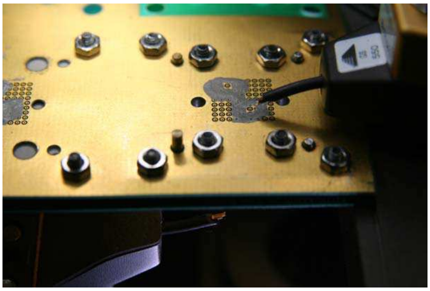

Figure 8. Configuration of double-side probe station.

in Figs. 6(a) and 6(b), the phase of S_{21} is -3.65 degree at 1 GHz and equals 10.13 pico second thru delay. The difference between the novel double-side and conventional thru element is the embedding of CPW inside dielectric layers that connects the probes at above and below the sides. The other calibration elements like open, short, and loading from supplier are available for each single port calibration.

A customized probe station as shown in Fig. 7 is necessary for the novel 3D calibration and measurement. A microscope on the top observes top side patterns, and an image sensor on the bottom observes backside patterns. One arm has been rotated 180 degrees to aim the probe at the top as shown in Fig. 8.

In this research, the measurement of data depends on an Agilent E5071C with a sweep frequency ranging from 100 MHz to 6 GHz.

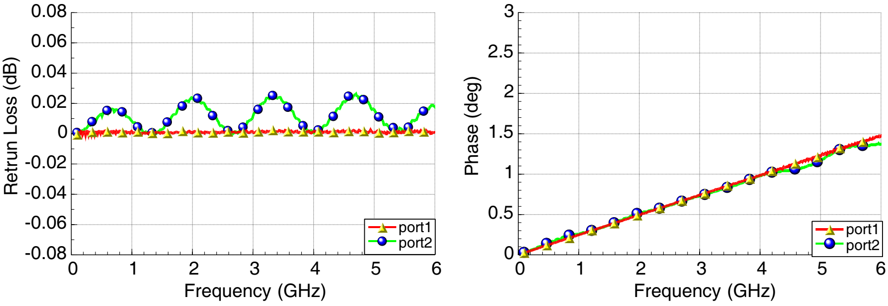

(a) (b)

Figure 9. (a) Return Loss of the open standard. (b) Phase of the open standard.

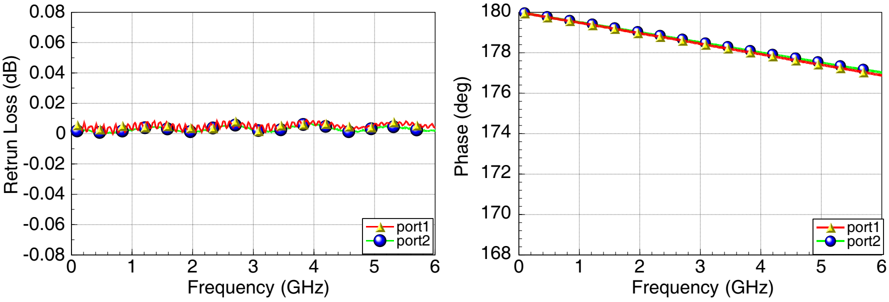

(a) (b)

Figure 10. (a) Return Loss of the open standard. (b) Phase of the open standard.

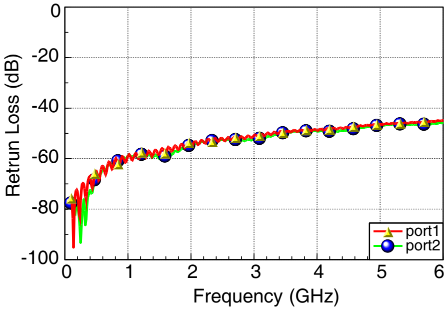

Figure 11. Return Loss of the load standard.

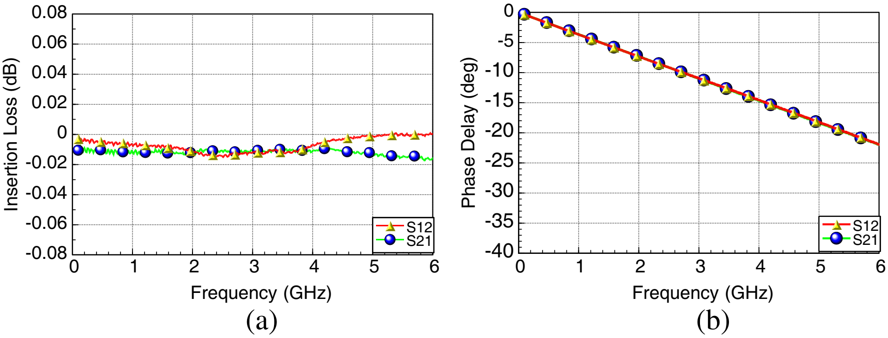

(a) (b)

Figure 12. (a) Insertion Loss of the thru standard. (b) Phase delay of the thru standard.

The RF probe ACP-40-GS-550 by Cascade is applied to these measurements.

After the calibration is done, calibration standards are reconnected to ensure the quality of calibration. Novel double-side calibration results are presented in Figs. 9(a)–12(b). The return loss of measured open standard is almost less than a harsh specification of 0.02 dB. The cable vibration on the top side probe arm, port 2, causes resonance in Fig. 9(a). The phase of the measured open standard arising from 0 degree presents capacitance effect as shown in Fig. 9(b). The return loss of the short standard is almost zero as shown in Fig. 10(a), and the total reflection with short standard causing initial phase is 180 degree in Fig. 10(b). The return loss of measured load standard is less than −40 dB as shown in Fig. 11, which presents none reflection. The insertion loss of novel double-side thru standard is between 0.02 and −0.02 dB as shown in Fig. 12(a), which shows great propagation between the ports. The phase delay as shown in Fig. 12(b) is −3.662

degree at 1 GHz, which matches the simulation result in Fig. 6(b). This verification presents high quality of novel double-side calibration.

3.2. Comparing Novel Double-side Measurement and Modeling Method

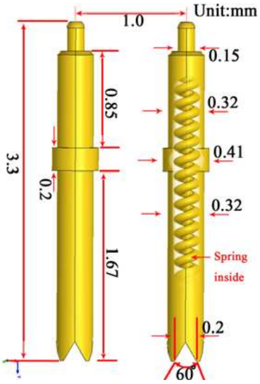

Figure 13. Detail structure of spring probe.

The spring probes are provided by C.C.P Contact Probe Co., Ltd. The spring probe structure shown in Fig. 13 shows the position of one signal pin and another ground pin with pitch of 1.0 mm. The two configurations must tighten all screws on the fixture and loosen two screws beside the spring probes (see the highlight in Fig. 2(b)). This represents each time compressing spring probe to working length and indicates a compression error.

The comparisons between the novel 3D direct measurement and conventional modeling method are presented in Figs. 14(a), 14(b), 14(c). The results of double-side measurement and models are similar, but this comparison shows parasitical effects that the models did not capture after 3.6 GHz. This error arises from the inaccuracy of inductance on the ground path and brings transmission drop down at higher frequency. This mismatch could be worsened if L_g is ignored as the modeling flow. Notice that there are reliability issues with the spring probe when testing with the wrong probe length and poor contacts. Loosening screws is increasing self and mutual inductance, also leads to resonant at lower frequency as shown in Fig. 14(a). The return losses are similar in Fig. 14(b), but the nonlinear phase delay of loosening screws is obvious in Fig. 14(c).

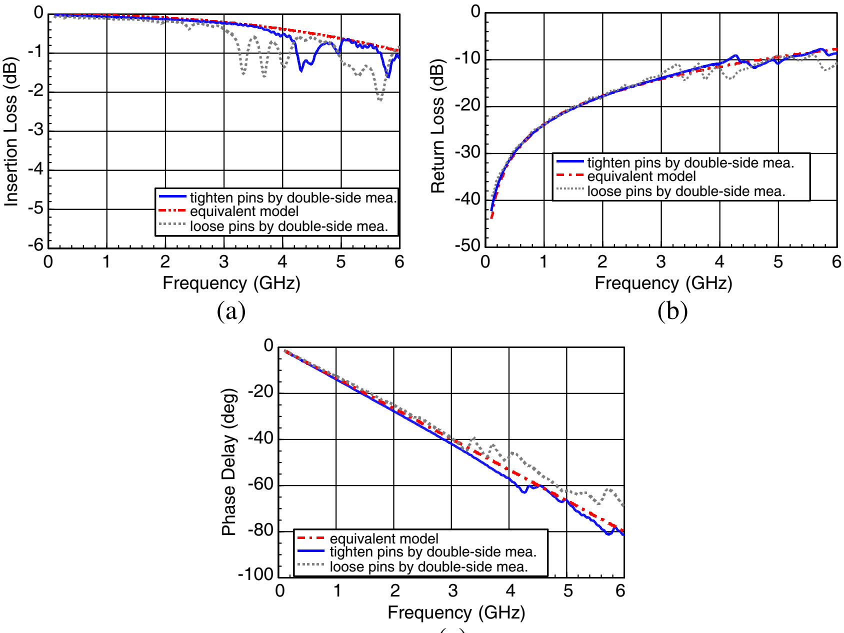

(a) (b)

(c)

Figure 14. (a) Insertion loss of modeling, 3D direct measured tighten and loose spring probes. (b) Return loss of modeling, 3D direct measured tighten and loose spring probes. (c) Phase delay of modeling, 3D direct measured tighten and loose spring probes.

4. CONCLUSION

The two approaches realize the characteristic of spring probe, the modeling methods with microwaves on-wafer measurements and a novel 3D direct calibrated measurement. The modeling method is unreliable because there are many steps and fixtures with model optimization. This method becomes complex to realize the characteristics of spring probes in real time. The advantage of the novel 3D measurement is realizing the characteristic of DUT directly and by comparing the modeling method, which proves the capability of 3D direct measurements.

In the future, 3D direct measurement will be developed into different pitches of type probe measurements that are applied to whole system testing, which contains die, package, and PCB. The pads on the die are small pitched with GSG type probes. Conversely, a wide pitch GS type probe is commonly used on the PCB. The most important application of 3D direct measurement is 3DIC and includes die stacked with TSV.

REFERENCES

1. Chen, M. K., C. C. Tai, Y. J. Huang, and L. K. Fang, "Electrical characterization of BGA test socket for high-speed applications," *Proceedings of the 4th International Symposium on Electronic Materials and Packaging, 2002*, 123–126, 2002.
2. Barnes, H., J. Moreira, H. Ossoinig, M. Wollitzer, T. Schmid, and T. Ming, "Development of a pogo pin assembly and via design for multi-gigabit interfaces on automated test equipment," *Asia-Pacific Microwave Conference, 2006. APMC 2006*, 381–384, 2006.
3. Szendrenyi, B. B., H. Barnes, J. Moreira, M. Wollitzer, T. Schmid, and T. Ming, "Addressing the broadband crosstalk challenges of pogo pin type interfaces for high-density high-speed digital applications," *IEEE/MTT-S International Microwave Symposium, 2007*, 2209–2212, 2007.
4. Sun, R.-B., C.-Y. Wen, Y.-C. Chang, and R.-B. Wu "A new isolation structure for crosstalk reduction of pogo pins in a test socket," *IEEE 18th Conference on Electrical Performance of Electronic Packaging and Systems, 2009. EPEPS'09*, 227–230, 2009.
5. Sun, R.-B., R.-B. Wu, and S.-W. Haiso, "Compromised impedance match design for signal integrity of pogo pins structures with different signal-ground patterns," *IEEE Workshop on Signal Propagation on Interconnects, 2009. SPI'09*, 1–4, 2009.
6. Horng, T. S., S. M. Wu, and C. Shih, "Electrical modeling of RFIC packages up to 12 GHz," *1999 Proceedings. 49th Electronic Components and Technology Conference*, 867–872, 1999.
7. Mukerji, S. K., G. K. Singh, S. K. Goel, and S. Manuja, "A theoretical study of electromagnetic transients in a large conducting plate due to current impact excitation," *Progress In Electromagnetics Research*, Vol. 76, 15–29, 2007.
8. Mukerji, S. K., G. K. Singh, S. K. Goel, and S. Manuja, "A theoretical study of electromagnetic transients in a large plate due to voltage impact excitation," *Progress In Electromagnetics Research*, Vol. 78, 377–392, 2008.
9. Kruppa, W. and K. F. Sodomsky, "An explicit solution for the scattering parameters of a linear two-port measured with an imperfect test set (Correspondence)," *IEEE Transactions on Microwave Theory and Techniques*, Vol. 19, 122–123, 1971.
10. Hiebel, M., *Fundamentals of Vector Network Analysis*, 1st edition, Rohde & Schwarz, 2007.